






 Cite this: *RSC Adv.*, 2020, 10, 22891

The synthesis, characterization, DNA/BSA/HSA interactions, molecular modeling, antibacterial properties, and *in vitro* cytotoxic activities of novel parent and niosome nano-encapsulated Ho(III) complexes†

 Deng Yinhu, ^{ab} Mohammad Mehdi Foroughi, ^c Zahra Aramesh-Boroujeni,^d Shohreh Jahani, ^{*e} Mohadesh Peydayesh,^{*f} Fariba Borhani,^{*g} Mehrdad Khatami, ^{eh} Meysam Rohani,ⁱ Michal Dusek^j and Vaclav Eigner^l

Based on the importance of metal-centered complexes that can interact with DNA, this research focused on the synthesis of a new Ho(III) complex. This complex was isolated and characterized *via* elemental analysis, and FT-IR, fluorescence, and UV-vis spectroscopy. Additional confirmation of the Ho(III) complex structure was obtained *via* single-crystal X-ray diffraction. DNA interaction studies were carried out *via* circular dichroism (CD) spectroscopy, UV-vis absorption spectroscopy, viscosity measurements and emission spectroscopy; it was proposed that the metal complex acts as an effective DNA binder based on studies in the presence of fish DNA (FS-DNA), showing high binding affinity to DNA in the presence of hydrophobic and electron donating substituents. Also, the interactions of this complex with human (HSA) and bovine serum albumin (BSA) proteins were studied *via* fluorescence spectroscopy techniques and the obtained results reveal an excellent propensity for binding in both cases. Furthermore, the interactions of the Ho(III) complex with DNA, BSA and HSA were confirmed *via* molecular docking analysis. The antimicrobial activities of the Ho(III) complex were tested against Gram-negative bacteria and Gram-positive bacteria. In addition, a niosome nano-encapsulated Ho(III) complex was synthesized, and the parent and encapsulated complexes were evaluated as potential antitumor candidates. The main structure of the Ho(III) complex is maintained after encapsulation using niosome nanoparticles. The MTT method was used to assess the anticancer properties of the Ho(III) complex and its encapsulated form toward human lung carcinoma and breast cancer cell lines. The anticancer activity in the encapsulated form was more than that of the parent Ho(III) complex. In conclusion, these compounds could be considered as new antitumor candidates.

 Received 17th April 2020
 Accepted 25th May 2020

DOI: 10.1039/d0ra03436c

rsc.li/rsc-advances

1. Introduction

Today, cancer is a principal challenging human health issue and it is a primary target of therapeutic chemistry.^{1–3} Organic complexes and natural products are implemented in chemotherapy. However, numerous literature reports have noted that

organic drugs show enhanced activity when coordinated with metal fragments.⁴ Therefore, metal complexes are the center of attention as possible chemotherapeutic agents.⁵

The success of cisplatin and its analogues in treating numerous cancer cell lines has resulted in the development of inorganic metal-based drugs in the past few decades. However,

^aDepartment of Pharmacy, Hunan Provincial People's Hospital, Changsha 410005, P. R. China

^bDepartment of Pharmacy, The First Hospital Affiliated to Hunan Normal University, Changsha 410005, P. R. China

^cDepartment of Chemistry, Kerman Branch, Islamic Azad University, Kerman, Iran

^dDepartment of Clinical Laboratory, AlZahra Hospital, Isfahan University of Medical Sciences, Isfahan, Iran

^eNanobioelectrochemistry Research Center, Bam University of Medical Sciences, Bam, Iran. E-mail: shohreh_jahani@yahoo.com; Tel: +98 35331321750

^fClinical Research Center, Pastor Educational Hospital, Bam University of Medical Sciences, Bam, Iran. E-mail: drpeydayesh57@gmail.com

^gMedical Ethics and Law Research Center, Shahid Beheshti University of Medical Sciences, Tehran, Iran. E-mail: faribaborhani@msn.com

^hCell Therapy and Regenerative Medicine Comprehensive Center, Kerman University of Medical Sciences, Kerman, Iran

ⁱDepartment of Medicine, Medical School, Bam University of Medical Sciences, Bam, Iran

^jInstitute of Physics of the Czech Academy of Sciences, Na Slovance 2, 18221 Prague 8, Czech Republic

† Electronic supplementary information (ESI) available. CCDC 1882574. For ESI and crystallographic data in CIF or other electronic format see DOI: 10.1039/d0ra03436c



the uses of cisplatin are limited because of its side effects and the human body's resistance to this drug.⁶ Studies have mostly considered the novel synthesis of specific extremely functional metal-based drugs with reduced toxicity and more developed therapeutic characteristics.^{7,8}

Inner transition metal complexes are of interest in the coordination chemistry and bioinorganic fields. Numerous rare earth complexes have been implemented in the biomedical evaluation field as magnetic resonance imaging (MRI) contrast agents and as useful catalysts for the hydrolytic cleavage of phosphate ester bonds.^{9–14} Such rare earth complexes with organic ligands are of significant interest because of their structures and the possible usefulness of their luminescent characteristics. Due to specific biological and photophysical features, rare earth complexes have been implemented as biological probes in the fields of molecular biology and clinical chemistry. Various rare earth complexes can play a role in treating tumor cell lines. Due to their specific electron configurations, rare earth complexes are a source of inspiration for numerous efforts to design and synthesize possible antibacterial and anticancer agents.¹⁵ Rare earth complexes are able to directly interact with DNA or prevent complete DNA relaxation *via* topoisomerase inhibition.^{16,17}

DNA is considered a substantial target for small molecule drugs, namely platinum drugs that irreversibly connect with DNA *via* covalent binding whilst preventing enzyme self-repair. Moreover, numerous metal complexes can bind with DNA *via* non-covalent binding modes, such as intercalative, electrostatic and groove binding modes.^{18,19} Such binding interactions, alongside metal complex catalytic hydrolysis or oxidation, may destroy the DNA structure and cause the demise of carcinoma cells.²⁰

Human serum albumin (HSA) and bovine serum albumin (BSA) are the underlying elements of plasma proteins in humans and cows, correspondingly. HSA crystal formation analysis shows that drug binding sites are located in the IIA and IIIA subdomains.²¹ The geometry of the IIA pocket is rather different compared to that of IIIA, and a large hydrophobic cavity exists in IIA. BSA is homologous to HSA in terms of structure, with minor differences. HSA contains one tryptophan (Trp-214) within the IIA subdomain whilst BSA contains two tryptophan moieties (Trp-134 and Trp-213) in the IB and IIA subdomains, correspondingly.^{22,23}

HSA makes up a 60% share of the proteins within blood plasma and adopts a vital role concerning drug delivery whilst typically accumulating in tumor tissues.²⁴ Thus, a metal complex that binds to HSA may have enhanced anticancer and bioavailability activities.²⁵

The implementation of rare earth complexes as *in vitro* biomarkers and, in particular, binding probes is of considerable interest, and substantial progress can be expected in the future. This paper addresses the characterization and synthesis of a novel Ho(III) complex coordinated by the 2,2'-bipyridine (bpy) ligand: [Ho(bpy)(H₂O)₆]Cl₃. The crystal structure of the complex is ascertained *via* X-ray crystallography. The Ho(III) complex biological characteristics have been evaluated, including: (i) the study of the Ho(III) complex binding properties with FS-DNA *via* circular dichroism, emission titration and viscosity

measurements; (ii) competitive binding evaluations with ethidium bromine, which was studied *via* fluorescence spectroscopy, for the purpose of examining the possible intercalation of the Ho(III) complex with DNA; (iii) the study of the Ho(III) complex binding characteristics with HSA and BSA *via* UV-vis and fluorescence spectroscopy at three various temperatures, as well as *via* circular dichroism; (iv) molecular docking studies of the interactions of the complex with HSA, BSA and DNA; (v) the evaluation of the Ho(III) complex antimicrobial characteristics against Gram-positive bacteria and Gram-negative bacteria; (vi) and studies of the *in vitro* cytotoxic activity of the Ho(III) complex and its encapsulated forms against two human carcinoma cell lines (MCF-7 and A-549) *via* MTT assays.

2. Experimental

2.1. Materials and instrumentation

In order to determine the FS-DNA solution concentration ($\epsilon_{260} = 6600 \text{ M}^{-1} \text{ cm}^{-1}$), as well as the purity ($A_{260}/A_{280} = 1.8\text{--}1.9$), UV-vis spectrometry was utilized, which could indicate a lack of protein contamination. Solutions of FS-DNA and the complex with tris(hydroxymethyl-aminomethane)-HCl buffer, possessing 50 mM NaCl and 5 mM Tris-HCl (pH \approx 7.2), were used to conduct tests relating to the interactions between FS-DNA and the complex. N, H and C content evaluations of the complex were conducted utilizing a PerkinElmer 2400 primary analyzer. The UV-vis absorption spectra were obtained *via* an Analytik Jena SPECORD S100 UV-vis spectrophotometer. At room temperature, fluorescence measurements were conducted using a PerkinElmer LS-3 spectrofluorophotometer that included 1 cm path length quartz cuvettes. An Aviv spectropolarimeter 215 model was used to record the CD spectra *via* a cylindrical cuvette with a 0.1 cm path length. The encapsulated version of the Ho(III) complex was analyzed using an inductively coupled plasma (ICP-Spectro ciros CCD instrument) spectrometer. By utilizing inductively coupled plasma measurements, the quantity of nano-encapsulated Ho(III) complex within the niosomes was ascertained. A LEO, LEO912-AB transmission electron microscope (TEM) and KYKY EM 3200 scanning electron microscope (SEM) were utilized to evaluate the surface morphology pertaining to the encapsulated version of the Ho(III) complex.

2.2. Synthesis and characterization of [Ho(bpy)(H₂O)₆]Cl₃

2.0 ml of ethanol solution was used to dissolve HoCl₃·6H₂O (1.0 mmol), and this was then added in a dropwise manner to 2,2'-bipyridine (1.0 mmol) ethanol solution. The resulting reaction mixture was refluxed for a period of 24 hours. After cooling down to room temperature, the resulting solution was filtered, and the white colored precipitate was gathered and washed three times using ethanol. Then, the resulting product was subjected to recrystallization from acetonitrile, taking the form of transparent crystals. Yield: 68.0%. Anal. calc. for C₁₀H₂₀N₂O₆HoCl₃: C, 22.43%; H, 3.73%; N, 5.23%; found: C, 22.26%, H, 3.61%; N, 5.17%. ¹H NMR (D₂O) ppm: 8.08, 7.82, 7.70 (broad, H-bpy).



2.3. X-ray data collection and crystallographic study

Ho(III) complex crystallographic data was gathered using a SuperNova diffractometer equipped with monochromated Mo-K α radiation (0.71073 Å). Direct methods were used to solve the crystal structure with the Superflip program²⁶ prior to refinement using the full matrix least squares F^2 method *via* the Jana 2006 program.²⁷ In various Fourier maps, hydrogen atoms were distinguished and refined to a rational geometry. Harmonic refinement was used to refine all non-hydrogen atoms. For further information on data collection and structure refinement, see Table 1.

2.4. DNA-binding experiments

2.4.1. Absorption titration. The complex was titrated against FS-DNA (0–9.9 μ M) at a constant complex concentration of 4×10^{-5} M in Tris–HCl buffer (pH \approx 7.2). Mixture equilibrium was ascertained for a period of 5 minutes before spectra were obtained. Equal volumes of FS-DNA were added to the reference solution and compound solution during the measurement process to allow for the removal of FS-DNA absorbance from the absorption spectra. Every specimen solution was scanned from 210 to 325 nm. Eqn (1) was used to derive the binding constant (K_b) for the Ho(III) complex according to the spectroscopic titration information:

$$[Q]/(\varepsilon_a - \varepsilon_f) = [Q]/(\varepsilon_b - \varepsilon_f) + 1/K_b(\varepsilon_b - \varepsilon_f) \quad (1)$$

where [Q] denotes the DNA concentration in the role of a quencher, whilst the evident extinction coefficient (ε_a) was acquired from calculating $A_{\text{obsd}}/[\text{Ho(III) complex}]$. The expressions ε_f and ε_b are associated with the extinction coefficients of free and bound metal complexes, respectively. The slope $1/(\varepsilon_b - \varepsilon_f)$ and intercept $1/K_b(\varepsilon_b - \varepsilon_f)$ are obtained by plotting $[Q]/(\varepsilon_a - \varepsilon_f)$ vs. [Q]. K_b denotes the slope to intercept ratio.

2.4.2. Fluorescence titration. Various FS-DNA solution (3.30×10^{-4} M) volumes were added to Tris–HCl buffer (pH \approx 7.2) and

Ho(III) complex solution (2×10^{-5} M), ensuring that the FS-DNA concentration was controlled within the 0–16.5 μ M range. Every test was carried out at room temperature after 5 minutes.

Eqn (2) is employed to derive the quantity of the binding constant and the number of binding sites from the emission spectra:

$$\log(F_0 - F/F) = \log K_b + n \log[Q] \quad (2)$$

where [Q] represents the DNA concentration as a quencher, and F and F_0 denote the fluorescence intensities of the stock solution possessing the complex in the existence and absence of FS-DNA, respectively.

The Stern–Volmer eqn (3) was used to analyze the quenching data:

$$F_0/F = 1 + K_{SV}[Q] \quad (3)$$

Quantification of the Ho(III) complex binding capabilities with DNA was carried out, with F_0 and F representing steady state fluorescence intensities in the existence and absence of a quencher, respectively. [Q] denotes the quenching agent concentration and K_{SV} represents the Stern–Volmer constant. The F_0/F ratio is mapped out vs. the quencher concentration in the form of a Stern–Volmer plot. The resulting slope depicts the Stern–Volmer constant in the case where there is a linear relationship.

2.4.3. Description of the thermodynamic parameters. The thermodynamic factor relative values, consisting of the entropy change (ΔS°), enthalpy change (ΔH°), and free energy change (ΔG°), were acquired at various temperatures to determine the binding mode, using eqn (4):

$$\ln K_b = -\frac{\Delta G^\circ}{RT} = -\frac{\Delta H^\circ}{R} \left(\frac{1}{T} \right) + \frac{\Delta S^\circ}{R} \quad (4)$$

ΔG° was obtained from eqn (5):

$$\Delta G^\circ = \Delta H^\circ - T\Delta S^\circ \quad (5)$$

2.4.4. Viscosity measurements. Using an Ubbelohde viscometer thermostated at $26(\pm 0.2)$ °C in a constant temperature bath, viscometric tests were conducted. The flow times were determined using a digital watch. The DNA solution viscosity was ascertained in the existence and absence of increasing quantities of the Ho(III) complex. With regards to measurements of DNA viscosity, DNA was disintegrated in Tris buffer to assemble a 3.3×10^{-4} M working solution. Then, the Ho(III) complex was added with increasing concentrations within the 1.0×10^{-5} M to 14.0×10^{-5} M range to attain [complex]/[DNA] ratios within the 0.03 to 0.42 range. Every specimen was measured three times to derive a mean time period. The data was recorded in the form $(\eta/\eta_0)^{1/3}$ vs. [complex]/[DNA], where η denotes the DNA viscosity including the complex and η_0 is the DNA viscosity. Values of viscosity were obtained based on the DNA-containing solution flow period (t) and the flow period of the buffer alone (t_0): $\eta = (t - t_0)/t_0$.²⁸

2.4.5. DNA circular dichroism measurements. For the purpose of recording DNA CD spectra, an Aviv 215 model

Table 1 Crystallography data for [Ho(bpy)(H₂O)₆Cl]₃

Complex	1
Empirical formula	C ₁₀ H ₂₀ HoN ₂ O ₆ ·3(Cl)
Formula weight	535.6
Crystal system	Triclinic
Space group	$P\bar{1}$
Crystal size (mm)	$0.50 \times 0.40 \times 0.28$
a (Å)	7.6541(6)
b (Å)	14.2569(15)
c (Å)	17.3435(11)
α (°)	89.723(7)
β (°)	87.557(6)
γ (°)	87.201(8)
V (Å ³)	1888.6(3)
Z	4
D_{calc} (g cm ⁻³)	1.884
T (K)	120
θ_{max} (°)	29.6
$R[F^2 > 3\sigma(F^2)]$, $wR(F^2)$	0.026, 0.047
$\Delta\rho_{\text{max}}$, $\Delta\rho_{\text{min}}$ (e Å ⁻³)	1.29, -1.00



spectropolarimeter was used in the existence and absence of the Ho(III) complex at room temperature, *i.e.* 25 °C, with a 0.1 cm path length quartz cell. At a scan speed of 200 nm min⁻¹, four scans were gathered and data were attained every 0.2 nm within the 220–320 nm range. Determining the average, CD spectra were attained at [Complex]/[DNA] ratios of 1/*R* = 0–0.1.

2.5. BSA- and HSA-binding experiments

BSA concentrated stock solution was obtained *via* dissolving a suitable quantity of BSA in Tris–HCl buffer (containing 5 mM Tris/50 mM NaCl at pH 7.2). The spectrophotometric determination of BSA concentration took place using the molar absorptivity relationship $\lambda_{280} = 44\,300\text{ M}^{-1}\text{ cm}^{-1}$.

Ho(III) complex and HAS stock solutions were assembled in Tris–HCl buffer (pH = 7.2). The HSA concentration was ascertained spectrophotometrically based on the molar absorptivity of 36 500 M⁻¹ cm⁻¹ at 280 nm. The HAS solutions were preserved at 4 °C under dark conditions and used after no more than 4 days.

2.5.1. Fluorescence titration. A fixed concentration of BSA (3.6×10^{-6} M) was titrated in fluorescence titration tests with the successive addition of Ho(III) complex stock solution within the 1.25×10^{-6} M to 16.25×10^{-6} M range. Fluorescence emission spectra were obtained at three temperatures (293, 298, and 303 K). The emission spectra were recorded within the 310–450 nm wavelength range with emission and excitation wavelengths of 349 nm and 280 nm, respectively.

HSA fluorescence quenching spectra were obtained by maintaining the HSA concentration at a constant value (1.57×10^{-5} M) whilst enhancing the concentration of Ho(III) complex (1.25×10^{-6} M to 15.0×10^{-6} M) at room temperature. The fluorescence quenching spectra were recorded from 290–510 nm, and the excitation wavelength was 280 nm.

2.5.2. Forster resonance energy transfer (FRET) study. FRET concerns non-radiative electromagnetic energy transfer to an acceptor quencher existing in the ground state, originating from a photoexcited donor fluorophore within its vicinity.²⁹ According to our research, the fluorophore protein is a donor and the quencher molecule is an acceptor.

The transferred energy was deduced *via* FRET theory²⁹ (implementing eqn (6)):

$$E = 1 - (F_0/F) = R_0^6/(R_0^6 + r^6) \quad (6)$$

where *E* is the energy transfer efficiency, *F*₀ is the pure BSA or HSA fluorescence intensity, *F* is the BSA or HSA fluorescence intensity in the presence of the quencher complex, and *r* is the binding site proximity among the quencher and fluorophore molecules. The Forster critical energy transfer distance (*R*₀) at which there is an energy transfer efficiency of 50% was derived *via* eqn (7):

$$R_0^6 = 8.79 \times 10^{25} K^2 N^{-4} \Phi J \quad (7)$$

where $K^2 = 2/3$ is the BSA and HSA spatial orientation factor, *N* = 1.336 is the average refractive index of the medium, $\Phi = 0.15$ is the fluorescence quantum yield,²⁹ and *J* is the overlap integral

of the absorption spectrum of the Ho(III) complex and the fluorescence emission spectra of BSA and HSA. Such a value was achieved by utilizing eqn (8):

$$J = \frac{\sum F(\lambda)\epsilon(\lambda)\lambda^4\Delta\lambda}{\sum F(\lambda)\Delta\lambda} \quad (8)$$

where *F*(λ) is the fluorophore BSA corrected fluorescence intensity in the wavelength range λ to $(\lambda + \Delta\lambda)$, and $\epsilon(\lambda)$ is the acceptor complex molar extinction coefficient at λ .²⁹

2.5.3. BSA and HSA circular dichroism measurements. Regarding the CD tests, the Ho(III) complex and BSA concentrations were 3.5×10^{-6} M and 3.5×10^{-6} M, respectively. The BSA spectra in the absence and presence of the Ho(III) complex were documented within the 200–250 nm range at 25 °C and with a 1 nm bandwidth, 1 nm step interval, 0.02 mm slit width, and average time of 0.5 s. For the purposes of data analysis, the Tris–HCl buffer spectrum was subtracted from the sample spectra.

HSA and Ho(III) complex concentrations were maintained at 2×10^{-6} and 2×10^{-6} M, respectively, for CD spectra measurements. These spectra were documented within the 200–270 nm range with a response time of 4 s and a scan rate of 200 nm min⁻¹. For every spectrum, three accumulated scans were used.

2.6. Docking protocol

To conduct docking calculations, the AutoDock 4.2.2 package was used. The Lamarckian genetic algorithm was used as a prominent search algorithm.³⁰ The HSA (PDB ID: 1BMO) and BSA (PDB ID: 3V03) crystal structures and d(CGCGAATTCGCG)₂ sequence dodecamer (PDB ID: 1BNA) DNA duplex information were downloaded from the Brookhaven Protein Data Bank. Hydrogen atoms and Gastiger charges were added to the protein structures and complex.³¹ During the docking procedure, BSA, DNA and HSA were kept stable whilst every torsional bond of the complex was freed. Spacing was induced *via* the AutoGrid program for a docking grip map of 80 × 80 × 80 points and a size of 0.375 Å. Thus, a maximum of 25 000 000 energy analysis calculations and 200 independent runs were implemented.

2.7. Antimicrobial assays

Antibacterial behavior was evaluated *via* the broth dilution technique against *P. aeruginosa* (ATCC 27853), *E. coli* (ATCC 25922), *K. pneumonia* (ATCC 10031), *S. typhi* (ATCC 1609), *E. VRE*, *Acinetobacter*, *E. faecium*, MRSA, and *faecalis* (ATCC 29212), which are causes of nosocomial infections. The bacterial growth intermediary used was Mueller–Hinton broth, including 2% glucose. The diameter of the inhibition zone was derived to acquire the Ho(III) complex antibacterial spectrum. A 10⁷ colony-forming units (CFU) per ml standard inoculum for the purpose of studying stains on a Muller–Hinton agar plate was produced *via* a swab prior to filter paper discs infused with antibacterial agents (6 mg ml⁻¹) being placed on the agar. Incubation was conducted at 37 °C overnight to calculate the inhibition zone diameter.



The minimal bactericidal concentration (MBC) and minimal inhibitory concentration (MIC) values, obtained *via* the broth mixture technique, were used to quantitatively derive the Ho(III) complex antibacterial behavior. A bacterial suspension (10^7 CFU mL^{-1}) was placed within test tubes of 5 ml of Mueller–Hinton broth containing complex mixtures within the 0.003–40 mg L^{-1} range. Incubation was conducted in an aerobic manner at 37 °C for a period of 24 hours. The non-shaken tubes were then evaluated to determine visible turbidity. The MIC denotes the lowest complex concentration without bacterial progression. Tests were conducted three times to validate the MIC results ($\mu\text{g mL}^{-1}$) pertaining to each strain. Upon the determination of the MIC value, 0.1 ml of inoculum solution from the tubes with visible turbidity was subjected to subculturing on a nutrient agar plate surface prior to incubation at 37 °C for a period of 24 hours. The resulting colony count on the subculture was compared with the CFU mL^{-1} count from the initial inoculum. MBC denotes the minimum complex concentration that permits less than 0.1% of the initial inoculum to survive.

2.8. Cytotoxicity

2.8.1. Preparation of the niosome nano-encapsulated Ho(III) complex. The niosome nano-encapsulated Ho(III) complex (NN-En-Ho) was prepared on the basis of previous studies (see Fig. 1).³²

2.8.2. Antitumor activity *in vitro* assays. The antitumor activities of the Ho(III) complex and NN-En-Ho against A-549 and MCF-7 cell lines were assessed using MTT assays *in vitro*, *via* an RPMI 1640 intermediary complemented with 10% FBS and 50 lg mL^{-1} penicillin–streptomycin. The MCF-7 (5×10^3 cells per well) and A-549 cell line incubation procedures were performed within 96 well plates at 37 °C in a 5% CO_2 humidified incubator for a period of 24 h, individually and in the presence of various compound concentrations. Then, MTT dilution (12 mM, 10 μL) was performed in the wells, and incubation was commenced for a period of 4 h at 37 °C. For the next stage, the media was dispensed and phosphate buffered saline was used to wash the wells. DMSO (50 μL) was added and incubation was continued for 10 minutes. An ELISA reader (Bio-Tek, Elx 808, Germany) at $k = 545$ nm was used to derive the IC_{50} values after incubation based on eqn (9):

$$\% \text{ cell cytotoxicity} = [1 - \text{Abs}(\text{drug})/\text{Abs}(\text{control})] \times 100. \quad (9)$$

The IC_{50} values, denoting the concentration of drug leading to a 50% reduction in cellular viability, pertaining to the Ho(III) complex and NN-En-Ho were derived.

The MCF-7 and A-549 cell lines in cell culture medium (100 μL) possessing 0.12 μg of Ho(III) complex (100 μM concentration) or 1.58 μg of NN-En-Ho (equivalent to 0.12 μg of Ho(III) complex) were subjected to incubation for 24 h in a 5% CO_2 incubator. The resulting supernatant was dispensed, and the mixture, *i.e.* compound cells, was subjected to treatment *via* CHCl_3 , HNO_3 and the Ho(III) complex; holmium content levels and the amount of niosome nano-encapsulated derivative (NN-En-Ho) were ascertained *via* ICP. Tests were performed with four repetitions and the number of wells tested/dose was two.

3. Results and discussion

3.1. Characterization of the complex

3.1.1. Crystal structure. The asymmetric unit of the title compound consists of two crystallographically independent mononuclear complexes, $[\text{Ho}(\text{bpy})(\text{H}_2\text{O})_6]^{3+}$, with six chloride anions (see Fig. 2). The Ho(III) ion is coordinated to one bidentate bpy ligand and six water molecules, forming an N_2HoO_6 polyhedron (see Fig. S1†). The Ho–N and Ho–O bond lengths are normal and comparable to those in related Ho(III) complexes.^{33,34} In both complex moieties, the Ho–N bond lengths are longer than the Ho–O coordination bonds, with an average bond length of 2.487 Å for Ho–N and 2.335 Å for Ho–O. The Ho–N bonds show very small differences from the average value, with the shortest bond length being 2.479(5) Å and the longest bond length being 2.492(5) Å. The differences are more pronounced in the Ho–O bonds, with a shortest bond length of 2.302(3) Å and a longest bond length of 2.377(3) Å. For further information on selected bond lengths and angles, see Table S1.† The 3D packing of the structure is shown in Fig. S2.†

The hydrogen bonds are a driving force in the crystal structure formation, with a well-developed system of $\text{O–H}\cdots\text{Cl}$ hydrogen bonds forming plates in the structure and weaker $\text{C–H}\cdots\text{Cl}$ bonds connecting the plates together (see Fig. 3). For further information on the hydrogen bonds, see Table S2.†

In order to inspect the DNA, BSA and HSA interactions, the crystalline structure of the Ho(III) complex was ascertained, providing the Ho(III) complex structure for use in subsequent experiments. It is worth noting that the noncovalent interactions in the two complexes are identical, thus only one complex is focused on.

3.1.2. Spectral characterization. The IR spectrum of the Ho(III) complex was compared with the free ligand (bpy) to determine the changes that might have taken place upon complexation (Fig. S3†). The IR spectrum of the free ligand (bpy) exhibits characteristic (C=N), (C=C), and (C–H) bands, which appear at 1583–1579, 1453–1415, and 740 and 757 cm^{-1} , respectively. In the complex, the stretching vibrations of these groups shift slightly to lower wavenumbers (1582–1545, 1437–1400, and 737 and 752 cm^{-1} , respectively). Also, the spectrum of the Ho(III) complex show new absorptions in the regions of

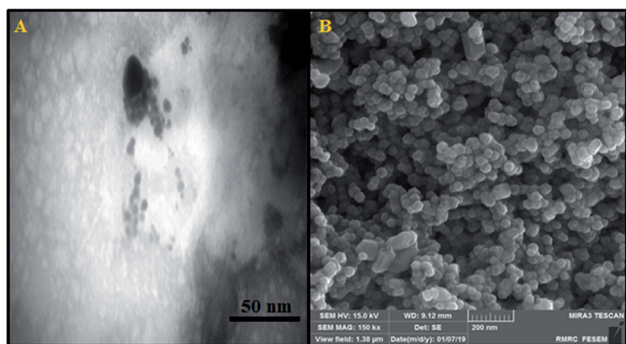
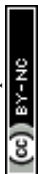


Fig. 1 (A) TEM and (B) SEM images of the niosome nano-encapsulated Ho(III) complex (NN-En-Ho).



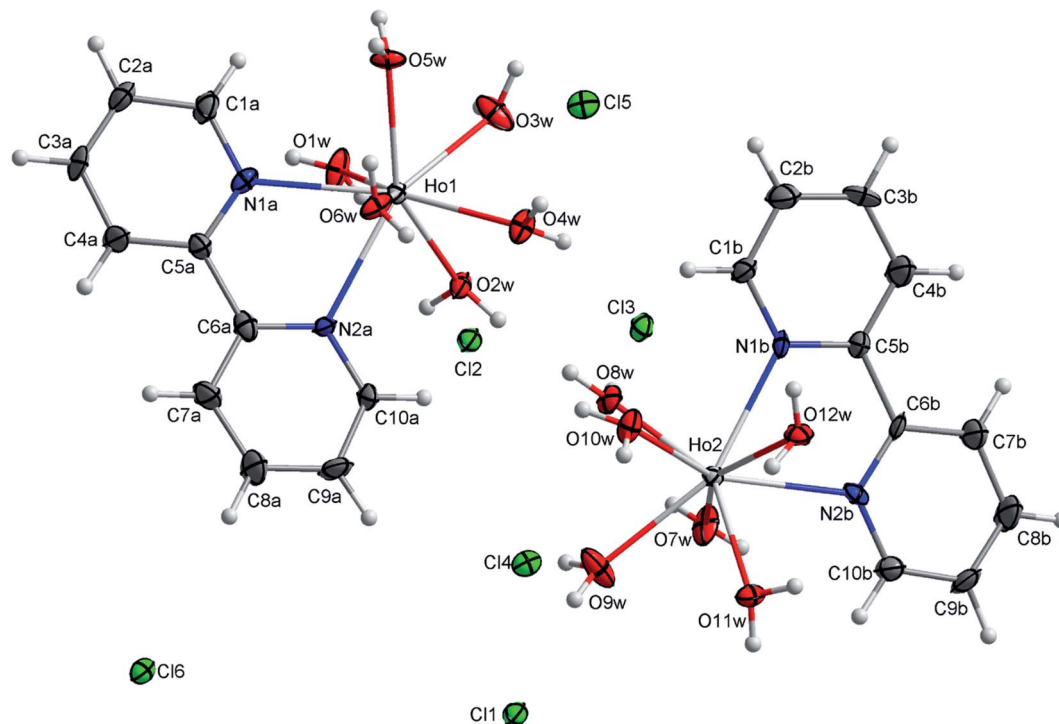


Fig. 2 An ORTEP view of the molecular structure of $[\text{Ho}(\text{bpy})(\text{H}_2\text{O})_6]\text{Cl}_3$ with ellipsoids drawn at the 50% probability level.

3550–2600, 414, and 1622 cm^{-1} , which are attributed to O–H and Ho–N stretching modes and the H–OH bending mode of H_2O coordination.

The f^{10} modification of Ho^{3+} involves 47 terms, creating 107 levels of different values of J due to spin orbit coupling. The $\text{Ho}(\text{III})$ ground state is $^5\text{I}_8$. The $\text{Ho}(\text{III})$ absorption spectrum in methanol is provided in Fig. S4a†. There were five evident multiplet-to-multiplet conversions from the ground state to $^5\text{G}_3$ and $^3\text{G}_5$ (Ho-I); $^5\text{G}_6$ (Ho-II); $^5\text{F}_2$ (Ho-III); $^5\text{S}_2$ and $^5\text{F}_4$ (Ho-IV); and $^5\text{F}_5$ (Ho-V) stimulated states in the case of the $\text{Ho}(\text{III})$ complex in the spectral range of 350 to 650 nm. Such conversions were assigned in the order of increasing conversion frequency. The most significant sensitivity towards the ligand and/or solvent atmosphere was evident in the case of the $^5\text{G}_6 \leftarrow ^5\text{I}_8$ centered absorption close to 438 nm, out of all the Ho^{3+} conversions seen during the study. Fig. S4b† shows the $\text{Ho}(\text{III})$ complex emission spectrum when subjected to an excitation wavelength of 280 nm at room temperature in methanol, documented within the 350 to 650 nm range. The four emission peaks at 430, 479, 561, and 638 nm, can be allocated to the $^5\text{G}_3 + ^3\text{G}_5 \rightarrow ^5\text{I}_8$, $^5\text{G}_6 \rightarrow ^5\text{I}_8$, $^5\text{S}_2 + ^5\text{F}_4 \rightarrow ^5\text{I}_8$, and $^5\text{F}_5 \rightarrow ^5\text{I}_8$ transitions of the Ho^{3+} ion, respectively. In regard to the ligand centered emission band (495 nm), there were no efficient transfers of energy from bpy to the Ho^{3+} center; thus, energy back-transfer from the Ho^{3+} ion became prominent.³⁵

3.2. DNA binding studies

3.2.1. Absorption titration. $\text{Ho}(\text{III})$ complex absorption spectra in the existence and absence of FS-DNA are presented in Fig. 4. The $\text{Ho}(\text{III})$ complex UV-vis spectra show the intense

ligand CT band and $\pi-\pi^*$ band within the 210 to 325 nm range, whilst the f–f band appears within the 350 to 650 nm range. Of the $\text{Ho}(\text{III})$ conversions, the excited J -level absorption intensity pertaining to the 4f configuration $\leftarrow ^5\text{I}_8$ centered close to the infrared area is significantly weak, *i.e.*, intra-configurational f–f transitions are forbidden in terms of parity with respect to the charge transfer transitions. Thus, DNA titration was conducted for the purpose of examining the charge transfer transitions. The rigidity of the $\text{Ho}(\text{III})$ complex was studied using UV-vis spectroscopy in Tris buffer for a period of 24 h at room temperature. There were no ligands discharged under such a state, thus the $\text{Ho}(\text{III})$ complex is considered stable.

The addition of FS-DNA to $\text{Ho}(\text{III})$ complex solutions at DNA/complex molar ratios within the range of 0 to 0.24 may lead to hypochromic shifts of between approximately 66.23% and 65.62% at 285 nm for the $\text{Ho}(\text{III})$ complex. Moreover, the $\text{Ho}(\text{III})$ complex absorption bands are reduced in intensity in the presence of increasing amounts of FS-DNA, showing the interactions among FS-DNA and the $\text{Ho}(\text{III})$ complex. The compound binding constant (K_b) was ascertained by utilizing eqn (1) to quantitatively acquire the $\text{Ho}(\text{III})$ complex binding strength with FS-DNA. A value of $0.6 \pm 0.02 \times 10^5 \text{ M}^{-1}$ was determined for the DNA binding constant (K_b). This value is lower compared to the recorded values for conventional intercalators (ethidium bromide: $K_b = 1.4 \times 10^6 \text{ M}^{-1}$; and $[\text{Ru}(\text{phen})\text{DPPZ}]^{2+}$: 10^6 to 10^7 M^{-1}).³⁶ Based on the results, the binding constant is higher when DNA groove binding is preserved.³⁷

3.2.2. Fluorescence spectra titration. The $\text{Ho}(\text{III})$ complex displayed a fluorescence maximum at $\lambda_{\text{em}} = 374 \text{ nm}$ upon excitement at $\lambda_{\text{ex}} = 280 \text{ nm}$. The fluorescence properties of the



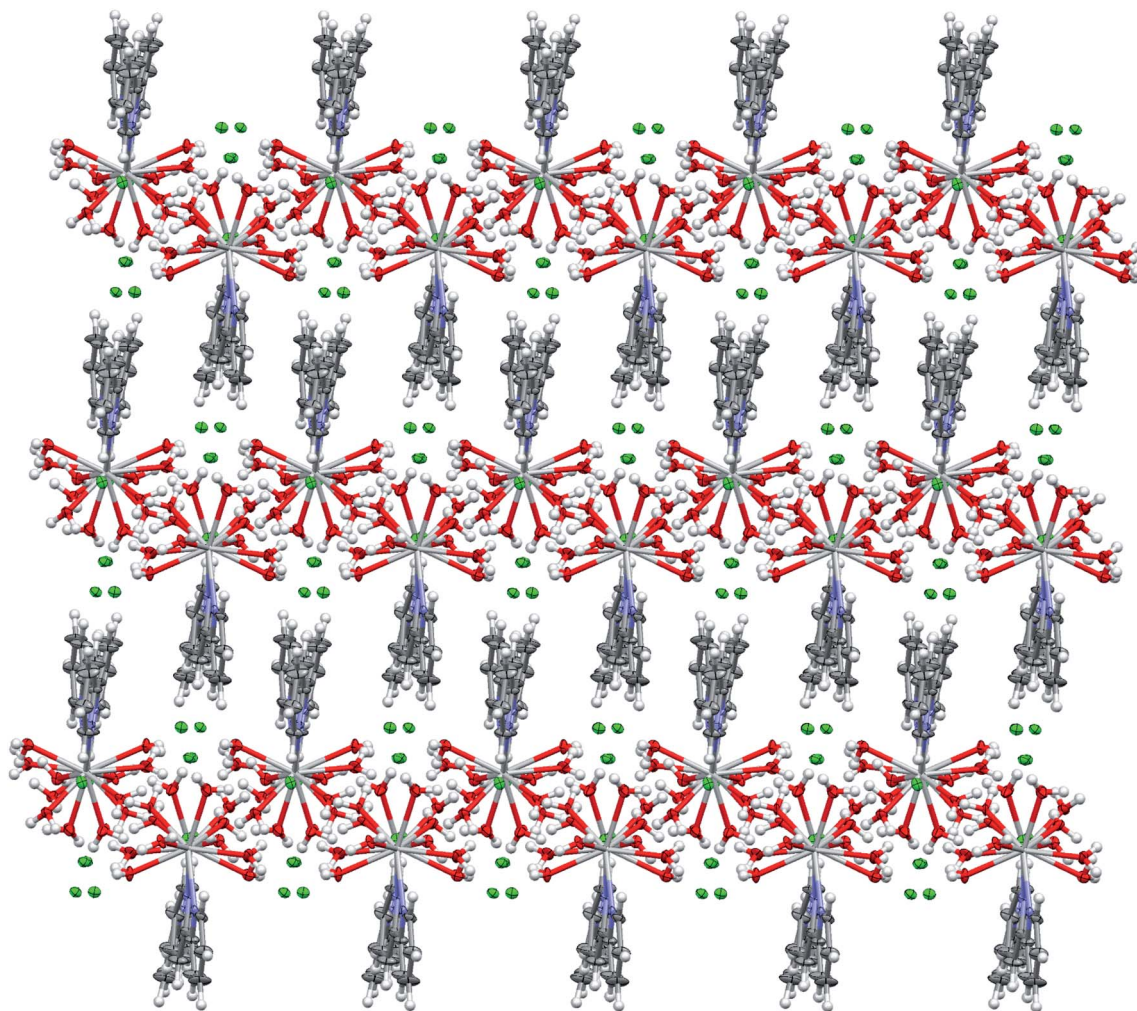


Fig. 3 The packing structure of $[\text{Ho}(\text{bpy})(\text{H}_2\text{O})_6]\text{Cl}_3$.

complex in CH_3CN , $\text{CH}_3\text{-OH}$, and H_2O are examined. The fluorescence intensity of the $\text{Ho}(\text{III})$ complex evidently increased as the solvent polarity was enhanced from acetonitrile to water. The impact of the $\text{Ho}(\text{III})$ complex concentration on emission was examined in water. The empirical results showed that the optimal $\text{Ho}(\text{III})$ complex concentration was 2×10^{-5} M. The $\text{Ho}(\text{III})$ complex fluorescence characteristics were significantly stable; higher intensities were observed at $\text{pH} \leq 8.0$, and the maximal value was obtained when $\text{pH} = 7.0$. Hence, Tris-HCl buffer at $\text{pH} 7.2$ is recommended for future investigations.

A fluorescence titration approach is implemented to study the interaction patterns and for a quantitative comparison of the relationship between the complex and DNA. The luminescence titration technique was used to acquire the binding constant of the $\text{Ho}(\text{III})$ complex to DNA. The reduction of the $\text{Ho}(\text{III})$ complex emission intensity upon the addition of FS-DNA is presented in Fig. 5. The binding site number (n) and K_b values are determined *via* plotting $\log(F_0 - F/F)$ against $\log[\text{DNA}]$, obtaining a linear plot. The K_b and n values pertaining to the $\text{Ho}(\text{III})$ complex were derived to be $3.8 \pm 0.03 \times 10^5 \text{ M}^{-1}$ and 1.05, respectively.

3.2.3. EB-DNA competition experiments. The binding mode of the complex with DNA was monitored using a fluorescent EB competitive assay. The fluorescence intensity of EB improves when DNA is added because of the significant intercalation of EB with DNA. The improved fluorescence may be subject to quenching when a second competitive molecule is added, as it may take the place of the EB and bind to DNA.³⁷ DNA-bound EB emission spectra in the presence and absence of the $\text{Ho}(\text{III})$ complex ($\lambda_{\text{ex}} = 525 \text{ nm}$, $\lambda_{\text{em}} = 555\text{-}650 \text{ nm}$) are shown in Fig. 6. When the $\text{Ho}(\text{III})$ complex is added to DNA pretreated with EB, substantial reductions in the emission intensity are attained, quenching the EB fluorescence. Upon this incorporation, the emission intensity of the EB-DNA system decreases by more than 50%, suggesting that the complex is bound to DNA *via* an intercalation mode when the ratio of the complex concentration to DNA is not over 100.³⁸ Adding the $\text{Ho}(\text{III})$ complex to DNA pretreated using EB at lower concentrations can reduce the intensity of emission by 22.33% (Fig. 6). This suggests that the $\text{Ho}(\text{III})$ complex is bound to DNA in an alternative mode from that of EB.



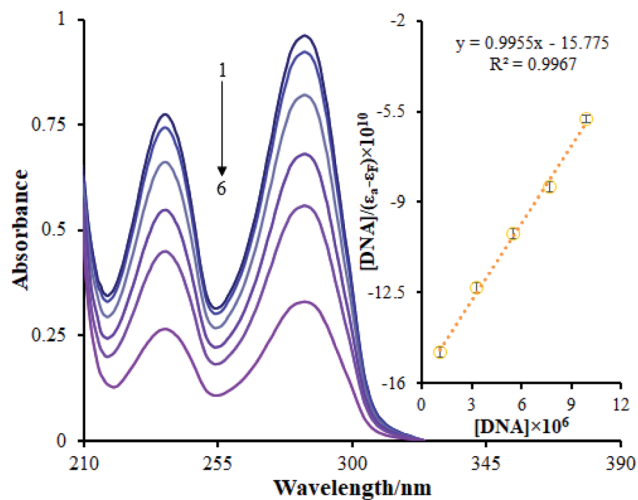


Fig. 4 UV-vis spectra of the Ho(III) complex (Tris-buffer, pH 7.2) in the absence and presence of increasing amounts (1 is lowest and 6 is highest) of FS-DNA; DNA concentrations: 0, 1.1, 3.3, 5.5, 7.7 and 9.9 μM ; inset: plot of $[\text{DNA}]/(\epsilon_a - \epsilon_f)$ versus $[\text{DNA}]$ during the titration of the complex with FS-DNA.

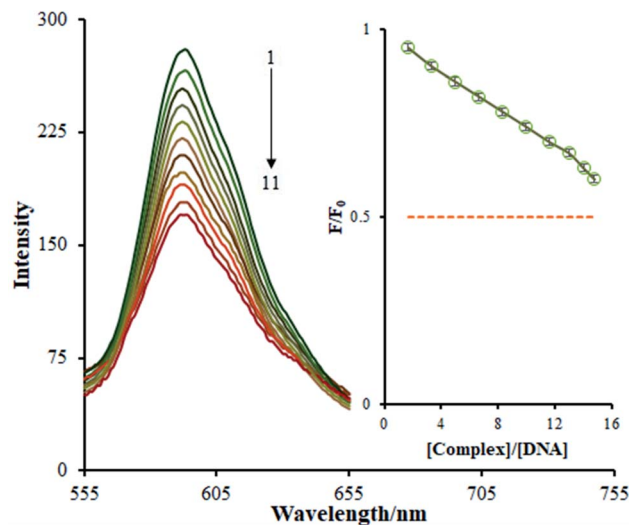


Fig. 6 The emission spectra of the DNA-EB system in the presence of increasing amounts (1 is lowest, 11 is highest) of the Ho(III) complex; inset: a plot of F/F_0 versus $[\text{Complex}]/[\text{DNA}]$.

3.2.4. Stern-Volmer quenching experiments. Various techniques may deactivate molecule fluorescence. The addition of a quencher to an excited molecule solution can cause a decrease in the intensity of fluorescence, based on either a state of equilibrium being formed with the non-fluorescent quencher complex, or contact *via* diffusion with the quencher. These techniques are static quenching and dynamic quenching. Various dependencies on temperature may allow static and dynamic quenching to be differentiated. The dynamic quenching procedure is enhanced when the temperature is

increased due to the faster movement of molecules with increasing temperature, which leads to an enhanced probability of collision. Contrarily, the production of a complex causes static quenching, thus, increased temperatures reduce complex stability and lead to a reduction of fluorescent quenching.³⁹ Therefore, the Ho(III) complex binding constants with FS-DNA are acquired *via* fluorescent titration at various temperatures. Fig. 7a shows the relevant Stern-Volmer plots and Table 2 presents the K_{SV} values.

Eqn (3) was used to obtain K_{SV} values by utilizing the linear relationships at different temperatures. It was shown that there is only one possible quenching procedure. According to Table 2, the K_{SV} values are too large to occur because of dynamic quenching. Based on the outcomes, there is a specific interaction between FS-DNA and the Ho(III) complex, and the quenching technique is potentially a static procedure.

3.2.5. Salt concentration effects. An efficient approach to discern the type of binding between DNA and small molecules is the study of ionic stability. Cations pertaining to salts (Na^+) may make the DNA phosphate backbone negative charges become neutral. Na^+ covers the DNA surface affecting the ionic strength in the case that the compound is bound to DNA through an electrostatic interaction mode. Hence, the complex may encounter difficulties when converging on the DNA molecules, leading to a reduction in the interaction strength with DNA and the emission intensity.⁴⁰ Thus, the impact of NaCl (0.1–0.6 M) on the fluorescence of Ho(III) complex + FS-DNA was examined. The outcome indicated that the F_0/F value of $[\text{NaCl}]$ stayed at 1.0 and is autonomous from NaCl concentration, where F_0 and F are the Ho(III) complex + FS-DNA intensities in the presence and absence of NaCl, respectively. Therefore, it may be stated that Ho(III) complex interaction with FS-DNA will not take place *via* an electrostatic mode.

3.2.6. Description of the thermodynamic parameters. Upon determining the impact of entropy (ΔS°) and enthalpy

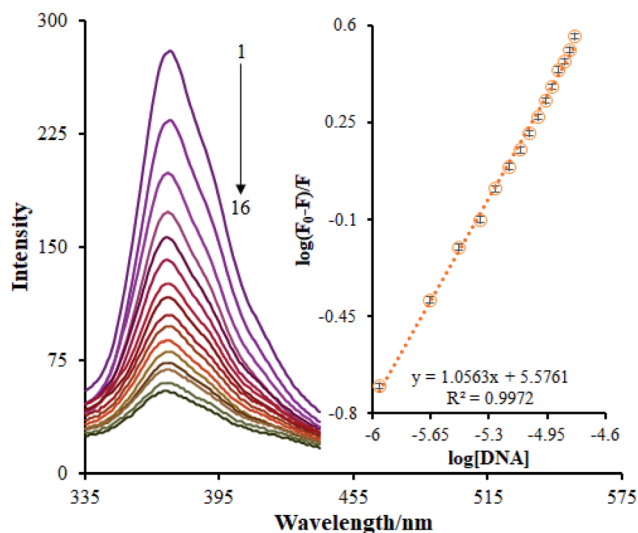


Fig. 5 The fluorescence spectra of complex-DNA; Ho(III) complex concentration: 2.0×10^{-5} M in Tris-buffer at pH 7.2; DNA concentrations (1 is lowest, 16 is highest): 0, 1.1, 2.2, 3.3, 4.4, 5.5, 6.6, 7.7, 8.8, 9.9, 11.0, 12.1, 13.2, 14.3, 15.4 and 16.5 μM ; inset: plot of $\log(F_0 - F)/F$ vs $\log[\text{DNA}]$.



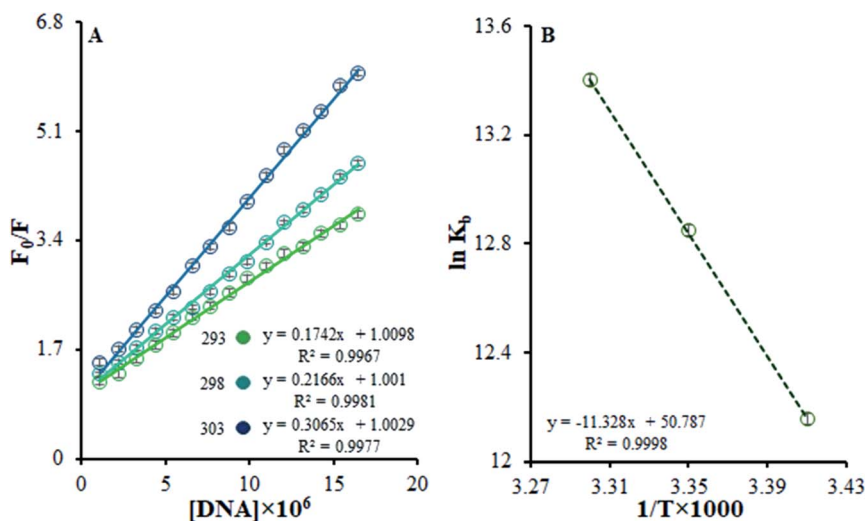


Fig. 7 (A) Stern–Volmer quenching plots of F_0/F versus $[DNA]$ in the temperature range of 293–303 K. (B) The van't Hoff plot for the interaction of the Ho(III) complex and DNA.

(ΔH°) changes, as shown in eqn (4), as well as free energy changes (ΔG°) through the van't Hoff equation (eqn (5)), on the reaction, the thermodynamics pertaining to reactions between FS-DNA and the Ho(III) complex may be perceived. Thus, the addition of the Ho(III) complex at different temperatures, *i.e.*, 293 K, 298 K, and 303 K, may be evaluated to acquire the thermodynamic factors, which include ΔS° and ΔH° , for DNA–complex formation *via* the van't Hoff equation and a plot of $\log(K_b)$ against $1/T$. The normal van't Hoff plot of $\ln(K_b)$ against $1/T$ for DNA bound to the Ho(III) complex in a relevant temperature range is presented by Fig. 7b. The slope of the plot determines the ΔH° value of the DNA binding response; the slope is equivalent to $-\Delta H^\circ/R$ where R denotes the gas constant. ΔS° for the reaction can be attained *via* the Y-intercept, which is equivalent to $\Delta S^\circ/R$.

Table 2 shows that, based on the ΔG° negative value and the exothermic nature of the reaction coinciding with the positive entropy and enthalpy variations, there is spontaneous binding between DNA and the Ho(III) complex.

The most prominent force binding FS-DNA to the Ho(III) complex is the hydrophobic interactions resulting from the positive values of ΔS° and ΔH° . Evidently, the entropy of origin

is the determining parameter influencing the stability of the DNA–complex. The discharge of counter ions or water molecules from the surface of the bound interacting partners may be determined during entropically driven DNA–complex interactions upon their binding, causing entropic gains. Adverse effects from enthalpy neutralize this impact due to the breaking of hydrogen bonds and non-covalent counter ion and water molecule interactions with non-complex partners. Furthermore, such interactions are enthalpically driven in the case of DNA intercalators and entropically driven in the case of groove binders.⁴⁰ The thermodynamic information displayed the importance of entropy during DNA–complex creation, whilst the role of enthalpy was less significant. To conclude, the Ho(III) complex interacts with FS-DNA through hydrophobic groove binding.

3.2.7. Viscosity studies. FS-DNA viscosity measurements were conducted *via* varying the concentration of added Ho(III) complex to highlight Ho(III) complex binding to DNA. The impact on the relative FS-DNA viscosity when supplemented with the Ho(III) complex was examined *via* utilizing the viscosity measurements, as shown in Fig. S5.†

Table 2 Stern–Volmer constants, binding data, and thermodynamic parameters of the DNA-, BSA- and HSA–Ho(III) complex systems at different temperatures

Temperature (K)	$K_{SV} \times 10^5$ (M^{-1})	$K_b \times 10^5$ (M^{-1})	ΔG° ($kJ mol^{-1}$)	ΔH° ($kJ mol^{-1}$)	ΔS° ($J mol^{-1} K^{-1}$)	
DNA	293	1.74 ± 0.02	1.9 ± 0.04	−29.47	94.18	422.24
	298	2.17 ± 0.04	3.8 ± 0.02	−31.57		
	303	3.06 ± 0.03	6.6 ± 0.03	−33.69		
BSA	293	2.21 ± 0.02	6.81 ± 0.02	−32.72	−34.07	−4.65
	298	1.93 ± 0.03	5.52 ± 0.05	−32.69		
	303	1.60 ± 0.02	4.29 ± 0.04	−32.67		
HSA	293	1.81 ± 0.03	8.35 ± 0.05	−33.33	−42.17	−32.31
	298	1.44 ± 0.03	6.42 ± 0.02	−33.17		
	303	1.19 ± 0.04	4.68 ± 0.02	−33.01		



The definition of intercalation is the insertion of a planar molecule among DNA base pairs, causing decreased DNA helical twisting and the extension of DNA. Thus, the lengthening and unwinding of the DNA helix in the presence of an intercalator may originate from base pairs dividing to adhere to the binding complex, hence enhancing DNA viscosity. To the contrary, there are no differences in the viscosity of DNA solution in the presence of agents that are bound to DNA through groove binding, and the twisting or bending of the DNA helix that may take place in the presence of agents that are electrostatically bound to DNA will decrease the viscosity and length concomitantly.²⁸ Prior examinations exist in regard to the impact of Ho(III) complexes on the viscosity of FS-DNA. A plot of the relative specific viscosity $(\eta/\eta_0)^{1/3}$ versus the [complex]/[DNA] ratio for the current complex exhibits no substantial variations in terms of viscosity. Thus, it can be concluded that interactions between FS-DNA and the Ho(III) complex take place *via* a groove-binding mode. The results of the viscosity tests validate the results from spectroscopic investigations.

3.2.8. CD spectroscopic studies. A potent method for determining DNA conformational changes related to interactions between DNA and small molecules is CD spectroscopy. The FS-DNA B-form conformation shows a negative band at 249 nm *via* right-handed helicity and at 279 nm it indicates a positive band *via* base stacking. Insignificant perturbations of helicity bands and base stacking may be evidence of electrostatic interactions and groove binding with complexes, whilst intensity variations pertaining to the two bands may be caused

by an intercalation mode, which stabilizes the DNA right-handed B conformation.⁴¹ The FS-DNA titrated Ho(III) complex CD spectrum is shown in Fig. 8a.

High Ho(III) complex concentrations decreased the positive and negative band concentrations but there were no changes in the shape; this shows that the DNA binding of FS-DNA with the Ho(III) complex induces specific conformational variances whilst reducing base stacking. The changes in the FS-DNA conformation originate from a transition from a B-type to a C-type formation in the DNA molecule, as shown in Fig. 8a. The viscosity and spectral evaluations are validated by the CD spectra investigations.

3.3. BSA and HSA binding studies

3.3.1. Fluorescence studies of BSA and HSA. One of the most useful ways of detecting the quenching mechanism, and binding strength, mode, and interactions between BSA and a compound is *via* fluorescence spectroscopy. The significant fluorescence characteristics of BSA are due to tryptophan and tyrosine amino acids. The intrinsic fluorescence intensity of BSA upon being excited at 280 nm mostly originates from tryptophan residues, Trp-212 and Trp-134, that are more exposed to the environment, and the amino acids, *i.e.* tyrosine and tryptophan, are excited.⁴² Fig. 9a depicts BSA fluorescence emission spectra in the presence and absence of the Ho(III) complex at $\lambda_{\text{ex}} = 295$ nm. It is clear that when the complex concentration is increased, there is a decrease in the BSA

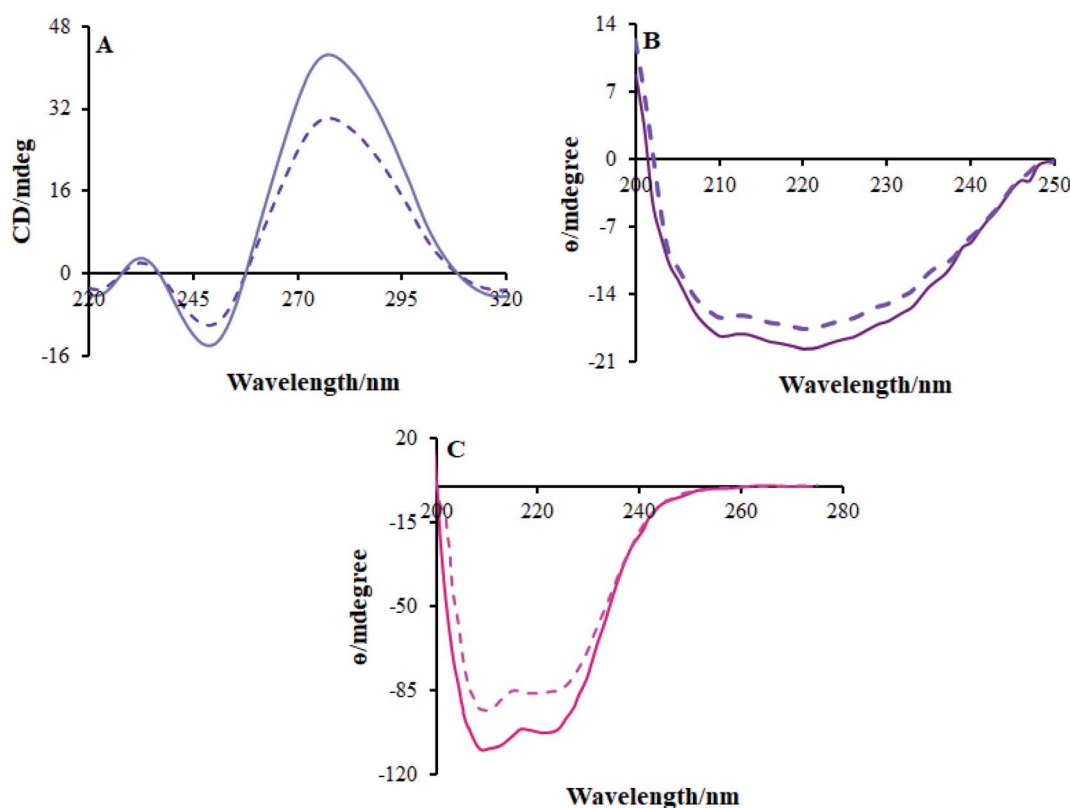


Fig. 8 CD spectra of (A) FS-DNA, (B) BSA and (C) HSA in the absence (solid line) and presence (dashed line) of the Ho(III) complex.



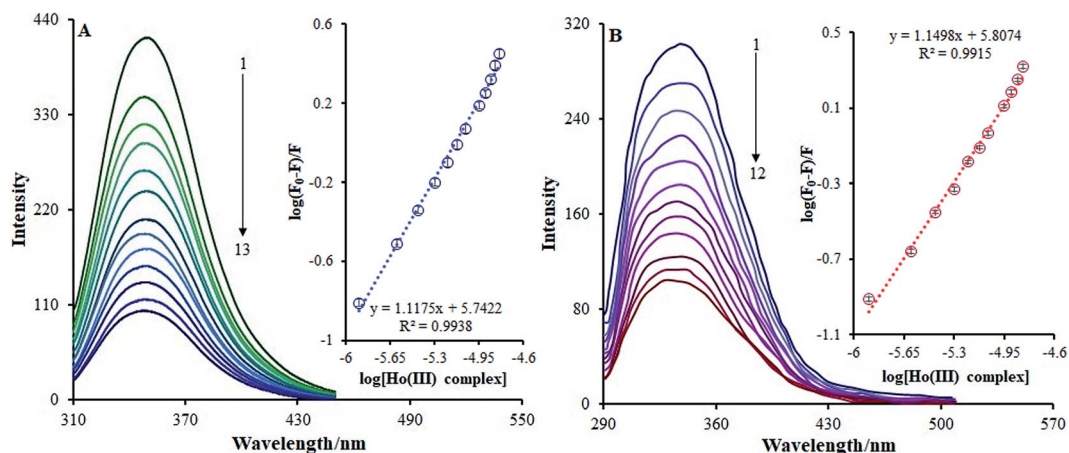


Fig. 9 (A) The fluorescence spectra of BSA–Ho(III) complex; BSA concentration: 3.6×10^{-6} M in Tris-buffer at pH 7.2; Ho(III) complex (1 is lowest, 13 is highest): 0, 1.25, 2.51, 3.75, 5.0, 6.25, 7.5, 8.75, 11.25, 12.5, 13.75 and 16.25 μM ; inset: plot of $\log[\text{Ho(III) complex}]$ vs. $\log(F_0 - F)/F$. (B) The fluorescent spectra of HSA–Ho(III) complex; HSA concentration: 1.57 μM in Tris-buffer at pH 7.2; Ho(III) complex (1 is lowest, 12 is highest): 0, 1.25, 2.51, 3.75, 5.0, 6.25, 7.5, 8.75, 11.25, 12.5, 13.75 and 15.0 μM ; inset: plot of $\log[\text{Ho(III) complex}]$ vs. $\log(F_0 - F)/F$.

fluorescence intensity with no substantial shift in the maximum emission wavelength position. The results show that the Ho(III) complex interacts with BSA, leading to the quenching of its intrinsic fluorescence. Moreover, such spectra are considered a useful method for establishing the BSA binding mode and strength, as well as the relevant quenching mechanism. Eqn (2) is implemented to derive the various binding parameters of the BSA–Ho(III) complex interactions.

In this case, F_0 and F are the BSA fluorescence emission intensities in the presence and absence of the Ho(III) complex, respectively, n is the quantity of binding sites, K_b is the binding constant, and Q is the Ho(III) concentration acting as a quencher. The calculation of $\log(K_b)$ can be conducted based on the intercept on a plot of $\log[(F_0/F)/F]$ versus $\log[Q]$ (inset Fig. 9a). Table 2 shows that the K_b value at 298 K is $5.52 \times 10^5 \text{ M}^{-1}$, and this is increased and decreased within the 293–303 K temperature range. It is noteworthy that a K_b value of 10^4 to 10^6 M^{-1} is suitable for drug–carrier complexes within the blood.⁴³ Thus, such a K_b value indicates that BSA can be regarded as a favorable carrier for transferring the Ho(III) complex *in vivo*.

Via utilizing a fluorescence approach, useful information relating to the interactions between HSA and metal complexes can be acquired, *e.g.*, binding modes, thermodynamic parameters, binding parameters, and the quenching mechanism.⁴⁴

Fig. 9b shows the HSA fluorescence quenching spectra in the presence or absence of the Ho(III) complex. At 337 nm, the fluorescence emission of the HSA characteristic broad band was quenched as the concentration of the Ho(III) complex increased. Such quenching may be accredited to possible variances in the HSA secondary structures, which indirectly indicates the binding of Ho(III) to HSA.

The binding constant (K_b) and number of binding sites (n) can be acquired using the adjusted Stern–Volmer equation (eqn (2)). Upon plotting $\log(F_0 - F)/F$ vs. $\log[Q]$ (Fig. 9b), the n and K_b values may be attained from the intercept and the slope of the double logarithm regression curve, and the relevant data are

given in Table 2. The value of K_b at room temperature was $6.42 \times 10^5 \text{ M}^{-1}$, showing that the amino acid side chain within the Ho(III) complex did not have any impact on the Ho(III) complex association constant with respect to HSA. Moreover, the HSA-binding constant proves that HSA may be regarded as a favorable carrier for transferring the Ho(III) complex *in vivo*.⁴⁴

3.3.2. Quenching mechanism. For the purpose of examining the quenching mechanism, the Stern–Volmer eqn (3) was used to analyze the fluorescence quenching data.

F_0 and F are the fluorescence intensities of BSA and HSA in the presence and absence of the quencher, respectively, $[Q]$ is the Ho(III) complex quencher concentration, and K_{SV} is the quenching constant.^{45,46} Fig. 10a and c depict F_0/F vs. $[\text{Ho(III) complex}]$ plots at various temperatures at $\lambda_{\text{ex}} = 295 \text{ nm}$. The K_{SV} values are acquired from the slopes of the plots of F_0/F vs. $[\text{Ho(III) complex}]$ at various temperatures.

The curves exhibit linearity within the range of experimental concentrations. This implies that there is only one type of quenching during the complex–BSA and HSA interactions.^{45,46} The derived K_{SV} values for the Ho(III) complex interactions with BSA and HSA at various temperatures are presented in Table 2. From this table, it is clear that the K_{SV} values are reduced when the temperature rises. Such results indicate the possible static nature of the quenching mechanism.

3.3.3. Determination of the thermodynamic parameters and the nature of the binding forces. Based on the binding constant values at the applied temperatures, the thermodynamic parameters and binding forces between the Ho(III) complex, and BSA and HSA are perceptible. The free energy change (ΔG°) during the binding interaction at various temperatures and the entropy (ΔS°) and enthalpy (ΔH°) changes are obtainable *via* the van't Hoff equation. In this vein, the thermodynamic parameters can be obtained from the relationship between $\ln(K_b)$ and the corresponding absolute temperature (eqn (4), Fig. 10b and d), such that K_b is the binding constant at the relevant temperature and R is the gas



constant. The entropy change (ΔS°) and enthalpy change (ΔH°) may be derived from the intercept and slope of the van't Hoff relationship, respectively. The free energy change (ΔG°) values were predicted using eqn (5). Table 2 summarizes the thermodynamic parameters arising from the interaction of the Ho(III) complex with BSA and HSA. It is clear from the negative values of ΔG° that the interaction process is spontaneous, whereas the negative values of ΔS° show the prominent roles of van der Waals forces and hydrogen bonds in the binding of BSA and HSA to the Ho(III) complex.^{46,47}

3.3.4. FRET studies. Fig. 11a shows the overlap integral of the BSA (1.58×10^{-6} M) fluorescence emission spectrum and the Ho(III) complex (1.58×10^{-6} M) absorption spectrum. Fig. 11b presents the overlap of the fluorescence emission spectrum of HSA (2.0×10^{-6} M) and the UV-vis spectrum of the Ho(III) complex (2.0×10^{-6} M). By implementing eqn (6)–(8), J ,

E , R_0 , and r values were derived, and the acquired values are presented in Table S3.†

Based on Förster resonance energy transfer theory,²⁹ the binding sites r must be within the vicinity of 2–8 nm in a state where $0.5R_0 < r < 1.5R_0$. The current results from the BSA and HSA–Ho(III) complex interactions satisfy the aforementioned condition, thus displaying the high potential for energy transfer from BSA and HSA molecules in the excited state to the ground state of the quencher complex. The FRET studies complement our research on BSA and HSA fluorescence quenching by the Ho(III) complex *via* a static mechanism.

3.3.5. Circular dichroism studies. Circular dichroism is a highly beneficial approach for analyzing protein secondary structures. For the purpose of verifying the binding mode, the BSA CD spectrum was documented in the presence and absence of the Ho(III) complex. Fig. 8b shows that the BSA CD spectrum

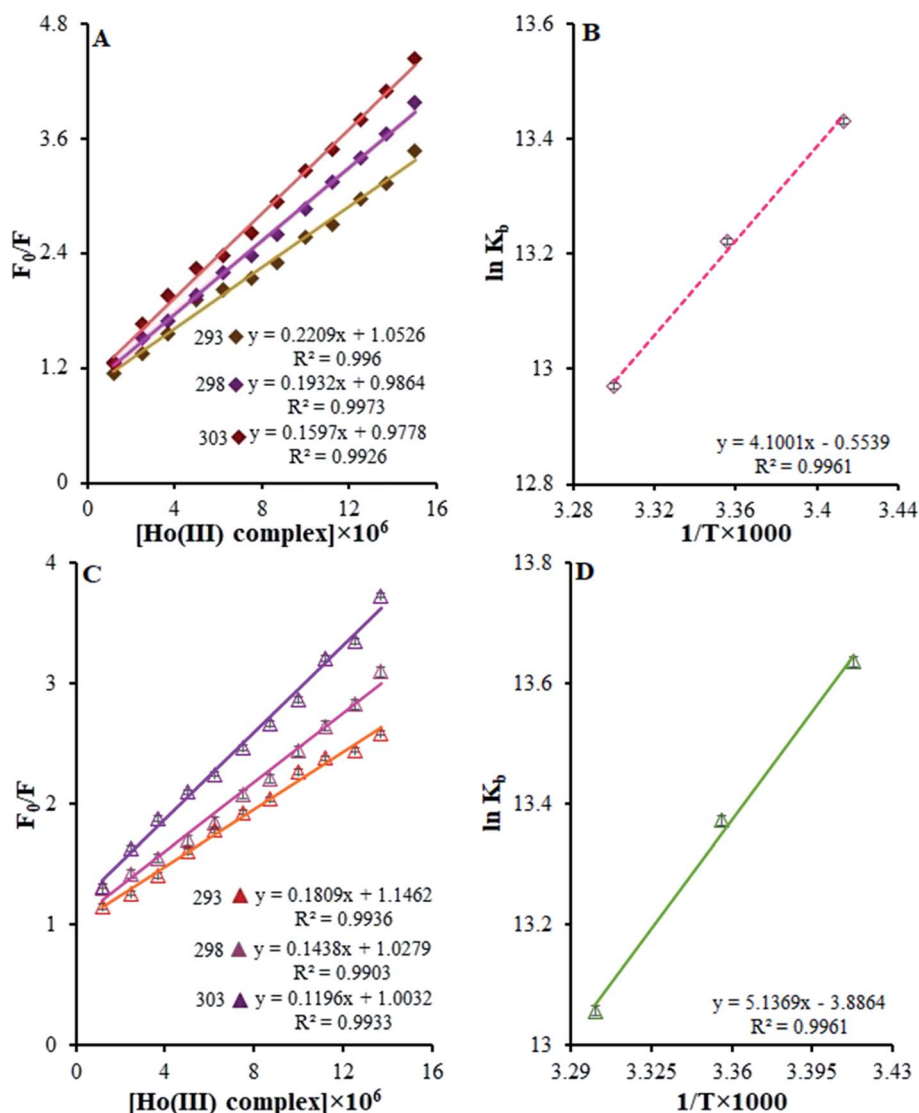


Fig. 10 (A) Stern–Volmer quenching plots of F_0/F versus $[\text{Ho(III) complex}]$ in the temperature range of 293–303 K. (B) The van't Hoff plot for the interaction of the Ho(III) complex with BSA. (C) Stern–Volmer quenching plots of F_0/F versus $[\text{Ho(III) complex}]$ in the temperature range of 293–303 K. (D) The van't Hoff plot for the interaction of the Ho(III) complex and HSA.



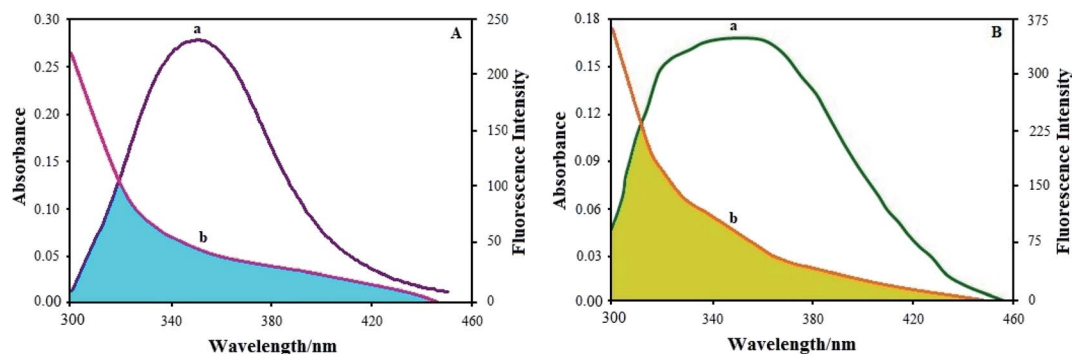


Fig. 11 (A) Overlap of the fluorescence spectrum of BSA ($T = 298$ K) and the UV absorption spectrum of the Ho(III) complex: (a) fluorescence spectrum of BSA; (b) UV absorption spectrum of the Ho(III) complex. (B) Overlap of the fluorescence spectrum of HSA ($T = 298$ K) and the UV absorption spectrum of the Ho(III) complex: (a) fluorescence spectrum of HSA; (b) UV absorption spectrum of the Ho(III) complex.

displays significant double minimum signals at 221 nm and 210 nm, which is an α -helix structural feature of the protein.⁴⁸ When the Ho(III) complex is added to BSA, the bands show reduced intensity, implying a reduction of the protein content in the α -helix structure.

CD spectroscopy is considered an influential method for studying variances in protein secondary structures after interactions with metallodrugs. The HSA CD spectrum displays two negative bands at 221 nm and 209 nm, which represent the usual protein α -helical structure because of the involvement of

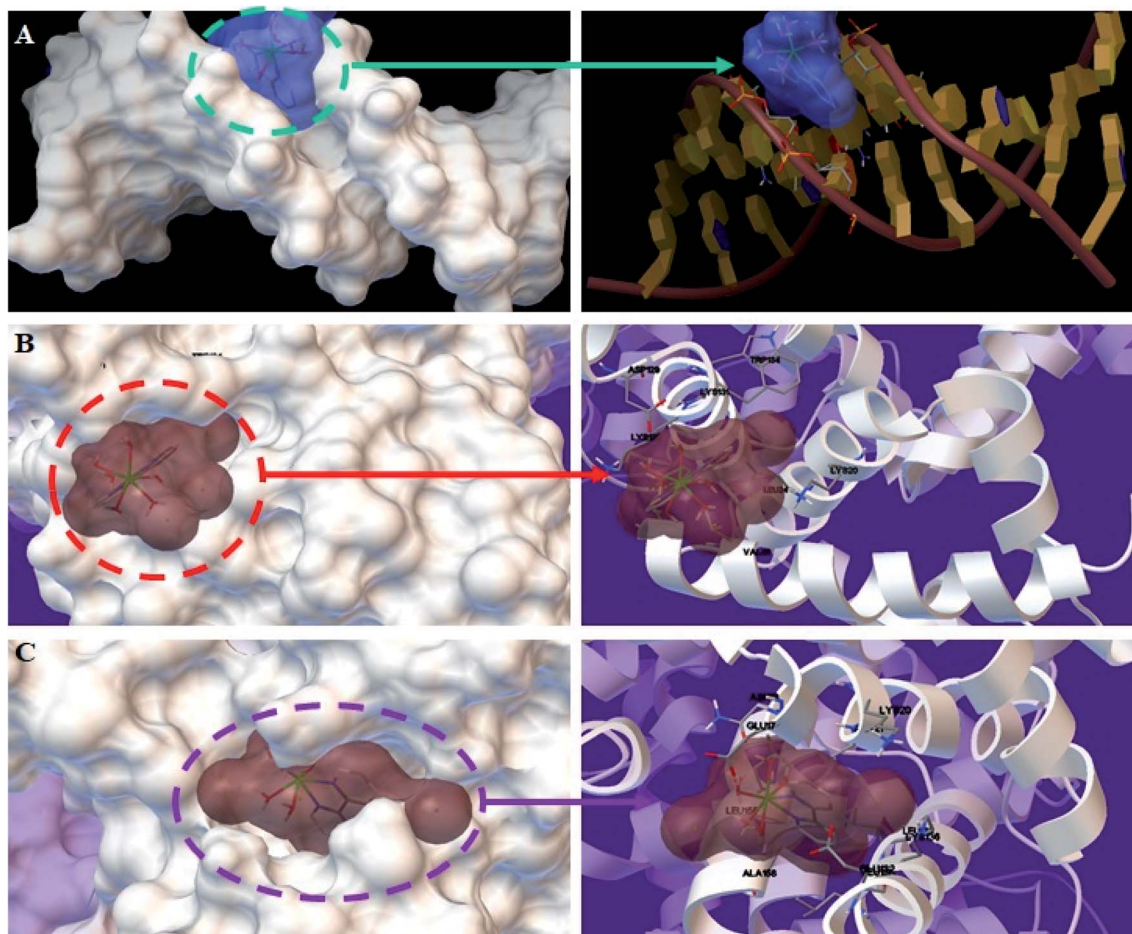


Fig. 12 Detailed view of the interactions between the Ho(III) complex and (A) DNA, (B) BSA, and (C) HSA. Only the more important residues for binding are shown.



$n \rightarrow \pi^*$ transfer in the peptide bonds of the α -helix, as shown in Fig. 8c. To gain insight into the variance of the HSA secondary structures once it interacted with the surfactant–Ho(III) complex, HSA CD spectra were documented in the presence and absence of the surfactant–Ho(III) complex.⁴⁶

3.4. Molecular docking results

3.4.1. Molecular docking with DNA. Molecular docking research is vital for drug discovery and structural molecular biology. The employment of highly automated docking software aids in the prediction of the binding mode, in addition to providing information regarding the structures of energetically beneficial complexes. The binding relationships between DNA and small molecules may be acquired easily from molecular docking research. The results from molecular docking proved that the Ho(III) complex possesses favorable binding energies, as shown in Table S3.† Fig. 12a shows that the Ho(III) complex reaches the gap between the DNA minor grooves mostly *via* the bpy ring.

The Ho(III) complex proved to have the best fit in the DNA minor groove, with a binding energy of $-5.31 \text{ kcal mol}^{-1}$. The energies acquired from docking research were in accordance with the obtained experimental results. The high negative energy suggests a formidable interaction between DNA and the Ho(III) complex, which was also shown through different spectral approaches. Thus, the docking results bolster the obtained experimental results and verify that a groove binding mode is operational between DNA and the Ho(III) complex.

3.4.2. Molecular docking with BSA and HSA. RMSD was the basis on which the docking results were clustered among the atom coordinates and they were ranked based on the binding energies. Lastly, the lowest binding energy structure and highest cluster members were documented. The results from molecular docking indicated that the Ho(III) complex exhibited comparatively adequate binding energies (Table S4†) and that it bound to BSA site 3 and HSA *via* a hydrophobic, L-shaped cavity in subdomain IB. The detailed interactions of the Ho(III) complex are presented in Fig. 12b and c. It is evident that the Ho(III) complex is in contact with a pocket of BSA surrounded by the hydrophobic residues LEU24, PHE36, VAL40, and TRP134, and in HSA it is surrounded by the hydrophobic residues ASN18, ALA21, LEU135, LEU139, LEU155, and ALA158. These

results are also in good agreement with the binding studies conducted through experiments and mentioned above.

3.5. Antibacterial effects

The antibacterial behavior of the Ho(III) complex is investigated based on inhibition region diameter measurements, and MBC and MIC methods. The inhibition region diameter range pertaining to the Ho(III) complex *versus* bacteria was within the 9.0 to 40.0 mm range, as shown in Table 3. The Ho(III) complex showed significant antibacterial behavior, namely *versus* *S. typhi*, VRE, and MRSA. Table 3 shows the adequate efficacy of the Ho(III) complex *versus* these bacteria. The MBC and MIC values of the Ho(III) complex *versus* bacteria were in the ranges of $0.14\text{--}4.0 \text{ mg ml}^{-1}$ and $14.0\text{--}125.0 \text{ }\mu\text{g ml}^{-1}$, respectively. Significant antibacterial behavior was shown by the Ho(III) complex with no consideration for Gram-class, especially toward MRSA, which is arduous to eliminate.⁴⁹ No antibacterial activity was shown by the ligand whilst using the Ho(III) complex as a biomaterial. The antibacterial behavior of the Ho(III) complex may be explained according to the chelation concept.⁴⁶ Metal ion polarity may be considerably condensed *via* chelation because the positive charge is partially shared with donor groups, and also due to the delocalization of electrons within the chelate ring. The condensation of metal ions may be intensified due to chelate lipophilic properties and interactions between the cell walls and metal ions. The charge dispersion and geometry of the metal complex molecules are consistent with bacterial cell walls, enhancing the penetration through the cell wall. Such unique structural adjustment can cause the collapse of the cell penetrability barrier and disrupt typical cell procedures. Interactions between cellular complexes and the metal ions are enhanced because of the diverse metal complex functional groups. The chelated complex may cause the deactivation of numerous cellular enzymes, modifying microorganism metabolic activity.⁵⁰

3.6. *In vitro* cytotoxicity studies

The MTT technique was utilized to evaluate the Ho(III) complex and NN-En-Ho antitumor behavior, assaying the behaviors of MCF-7 and A-549 cancer cell lines *in vitro*, as presented in Fig. 13 and 14.

Table 3 Zones of inhibition (mm) against bacteria of the Ho(III) complex, and MIC ($\mu\text{g ml}^{-1}$) and MBC (mg ml^{-1}) values of the Ho(III) complex toward bacteria

Bacteria	Zone of inhibition (mm)	MIC ($\mu\text{g ml}^{-1}$)	MBC (mg ml^{-1})
Gram-positive	<i>E. faecium</i>	15.0	125.0
	<i>E. faecalis</i>	9.0	125.0
	MRSA	40.0	14.0
	VRE	37.0	16.0
Gram-negative	<i>E. coli</i>	30.0	31.0
	<i>P. aeruginosa</i>	18.0	114.0
	<i>K. pneumoniae</i>	29.0	7.0
	<i>A. baumannii</i>	28.0	31.0
	<i>S. typhi</i>	34.0	16.0



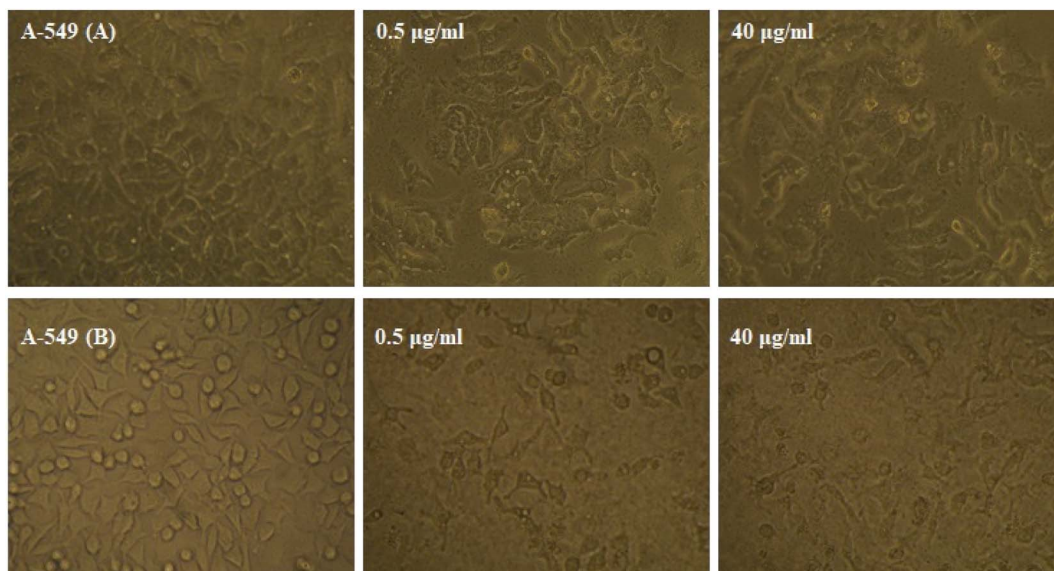


Fig. 13 Microscopic photographs of A-549 cancer cells in the absence and presence of different concentrations of the (A) Ho(III) complex and (B) niosome nano-encapsulated Ho(III) complex (NN-En-Ho) (concentrations are indicated by the number inside each photo).

Table S5† shows the inhibitory impact and IC_{50} values. The analysis results pertaining to variance indicate that the variations between the IC_{50} mean values of NN-EN-Ho and the Ho(III) complex with respect to both cell lines are statistically meaningful and not randomly created.

Furthermore, high levels of the compound groups produced identical results. The complex displays *in vitro* cytotoxicity versus the selected cell lines. Fig. 13 and 14 show that enhancing the concentrations of the complexes significantly reduces cancer cell proliferation, exhibiting a dose-reliant effect that hinders the growth of these cells.

Table S5† shows that the NN-En-Ho antitumor behavior is greater compared to the parent Ho(III) complex. The insertion of NN-En-Ho into the cell membrane occurs more effortlessly in comparison to the parent Ho(III) complex. Thus, it facilitates Ho(III) complex penetration into cancer cells whilst improving its antitumor behavior.

3.7. Comparison of the proposed complex with literature complexes

Table 4 presents a comparison of DNA/BSA/HSA binding in this research with other literature studies involving DNA/BSA/HSA

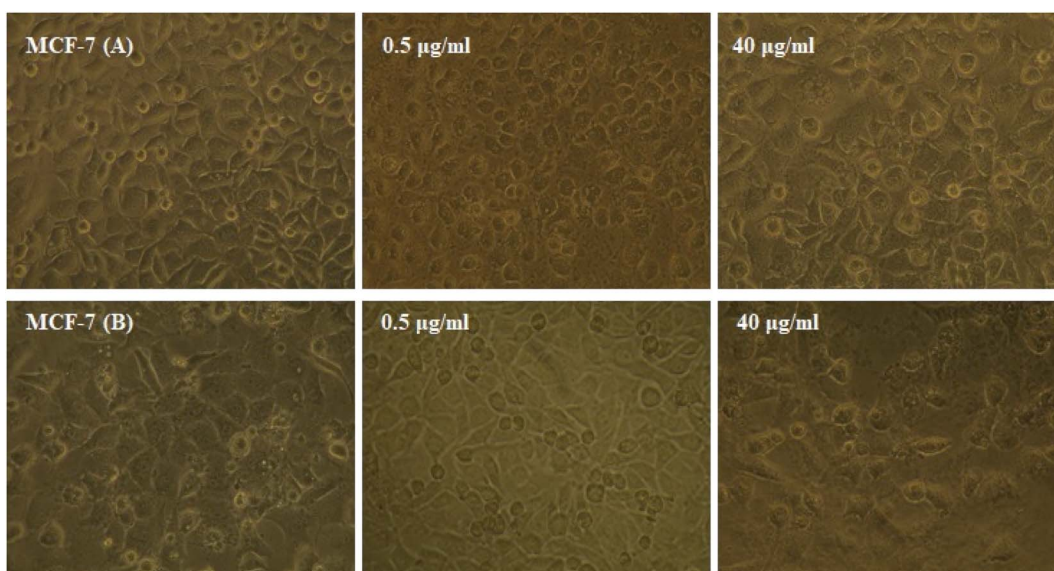


Fig. 14 Microscopic photographs of MCF-7 cancer cells in the absence and presence of different concentrations of the (A) Ho(III) complex and (B) niosome nano-encapsulated Ho(III) complex (NN-En-Ho) (concentrations are indicated by the number inside each photo).



Table 4 A comparison between various literature complexes and the proposed Ho(III) complex^a

Complex	$K_b \times 10^5 (M^{-1})$		$(IC_{50}) (\mu g ml^{-1})$		Ref.
	DNA	BSA	HSA	MCF-7	
[Ho(Neo) ₂ Cl ₃ ·H ₂ O]	6.12	—	—	5.66	35
[Ho(Phen) ₂ Cl ₃ ·H ₂ O]	0.107	—	—	—	51
[Eu(bpy) ₃ Cl ₃ (H ₂ O)]Cl	2.46	—	—	—	38
[Tb(bpy) ₃ Cl ₃ (OH ₂)]	1.01	—	3.63	—	52 and 53
[Yb(bpy) ₂ Cl ₃ ·OH ₂]	4.85	5.07	2.57	—	54 and 53
[Dy(bpy) ₃ Cl ₃ ·OH ₂]	2.30	1.18	2.95	—	55 and 53
[Ho(bpy)(H ₂ O) ₆]Cl ₃	3.80	5.52	6.42	7.23	This work

^a Neo: 2,9-dimethyl-1,10-phenanthroline; Phen: 1,10-phenanthroline; bpy: 2,2'-bipyridine.

binding.^{35,38,51,52} The proposed Ho(III) complex had larger K_b values in comparison to previously reported complexes in the literature, with the exception of two examples provided in ref. 35 and 54. The advantage of our research over ref. 35 is that we employ an inexpensive materials (bpy *versus* neo(2,9-dimethyl-1,10-phenanthroline)). In addition, in ref. 35, the interactions between BSA and HSA have not been investigated. Also, it is noteworthy that ref. 38 and 51–54 do not investigated the anticancer activities of the complexes or the construction of drug carriers. This proves that the Ho(III) complex in this study could be a favorable antitumor agent with more developed potential pharmaceutical functionality compared with the methods previously mentioned in the literature.

4. Conclusions

In the present study, independent [Ho(bpy)(H₂O)₆]³⁺ mononuclear complexes with six chloride anions were synthesized, exhibiting high binding affinity to FS-DNA. The interaction mechanism details were investigated for the binding of the Ho(III) complex to FS-DNA. Firstly, the interactions between the Ho(III) complex and FS-DNA were investigated *via* UV-vis and fluorescence methods under simulated physiological conditions. According to the presented findings, the intrinsic fluorescence of FS-DNA was quenched *via* a static quenching mechanism. Secondly, we studied the DNA-binding mode of the Ho(III) complex with FS-DNA. The results from EB-DNA competition and iodide quenching experiments, thermodynamic parameter studies, viscosity measurements, CD spectroscopy, and molecular docking studies suggested that the interaction mode between the Ho(III) complex and FS-DNA involves groove binding. The Ho(III) complex also shows good binding affinity with BSA and HSA. The fluorescence results show that the Ho(III) complex is a strong quencher and that it interacts with BSA and HSA through a dynamic quenching mechanism, as K_{SV} decreases with increasing temperature. The signs and magnitudes of the thermodynamic parameters (ΔH° , ΔS° and ΔG°) indicate that the main forces acting between BSA, HSA and the Ho(III) complex are van der Waals and hydrogen bonding forces. According to the results, BSA and HSA can act as carrier proteins for this complex. Moreover, we prepared the parent and encapsulated forms of the Ho(III) complex. All of these complexes revealed significant inhibitory impacts on the A-549 and MCF-7 cell lines; higher *in vitro* antitumor activity was found in the case of NN-En-Ho because of its higher cellular penetration. Accordingly, it can be said that niosomes are potent drug carriers for this complex, which can act as an effective antitumor agent. We hope that our findings will be helpful for generating knowledge regarding the mechanisms of interaction between small molecule compounds and FS-DNA, BSA and HSA, as well as for developing the potential biological, pharmaceutical and physiological functions of these compounds in the future.

Conflicts of interest

The authors declare that they have no known competing financial interests or personal relationships that could have appeared to influence the work reported in this paper.



Acknowledgements

This work was financially supported by Ren Shu Project of Hunan Provincial People's Hospital (RS201915). The crystallographic part was supported by Project 18-10504S of the Czech Science Foundation using instruments of the ASTRA lab established within the Operation program Pragu Competitiveness—Project CZ.2.16/3.1.00/24510.

References

- G. Morris, N. Pahad, H. W. Dirr and S. Fanucchi, *Arch. Biochem. Biophys.*, 2018, **657**, 56.
- M. Dickerson, B. Howerton, Y. Bae and E. C. Glazer, *J. Mater. Chem. B*, 2016, **4**, 394.
- W. Huang, Y. Liu, J. Wang, X. Yuan, H. W. Jin, L. R. Zhang, J. T. Zhang, Z. M. Liu and J. R. Cui, *Eur. J. Med. Chem.*, 2018, **157**, 887.
- S. Conoci, A. Mascali and F. Pappalardo, *RSC Adv.*, 2014, **4**, 2845.
- S. Komeda and A. Casini, *Curr. Top. Med. Chem.*, 2012, **12**, 219.
- C. X. Zhang and S. J. Lippard, *Curr. Opin. Chem. Biol.*, 2003, **7**, 481.
- P. Adak, B. Ghosh, A. Bauzá, A. Frontera, A. J. Blake, M. Corbella, C. D. Mukhopadhyay and S. K. Chattopadhyay, *RSC Adv.*, 2016, **6**, 86851.
- K. J. Barnham, C. J. Bauer, M. I. Djuran, M. A. Mazid, T. Rau and P. J. Sadler, *Inorg. Chem.*, 1995, **34**, 2826.
- T. Gyula, K. Zoltan and S. A. Dean, *Inorg. Chem.*, 2006, **45**, 9269.
- L. Luo, R. Xu, D. Zhao and S. Zhong, *J. Rare Earths*, 2010, **28**, 106.
- S. K. Agrawal and K. C. Gupta, *Indian J. Chem.*, 1988, **27**, 1008.
- T. R. Li, Z. Y. Yang, B. D. Wang and D. D. Qin, *Eur. J. Med. Chem.*, 2008, **43**, 1688.
- A. Zhu, Y. Zhou, Y. Wang, Q. Zhu, H. Liu, Z. Zhang and H. Lu, *J. Rare Earths*, 2018, **36**, 1272.
- S. Aime, S. G. Crich, E. Gianolio, G. B. Giovenzana, L. Tei and E. Terreno, *Coord. Chem. Rev.*, 2006, **250**, 1562.
- S. V. Eliseeva and J. C. G. Bunzli, *Chem. Soc. Rev.*, 2010, **39**, 189.
- T. F. Abbs Fen Reji, A. J. Pearl and B. A. Rosy, *J. Rare Earths*, 2013, **31**, 1009.
- Y. Li and Z. Yang, *J. Coord. Chem.*, 2010, **63**, 1960.
- P. M. Pithan, D. Decker, S. I. Druzhinin, H. Ihmels, H. Schönherr and Y. Voß, *RSC Adv.*, 2017, **7**, 10660.
- D. Inci, R. Aydn, Ö. Vatan, T. Sevgi, D. Y. Imaz, Y. Zorlu, B. Çosut, E. Demirkan and N. Çink, *J. Biol. Inorg. Chem.*, 2017, **22**, 1.
- M. Raza, Y. Wei, Y. Jiang, A. Ahmad, S. Raza, S. Ullah, Y. Han, Q. Ullah Khan and Q. Yuan, *New J. Chem.*, 2017, **41**, 8203.
- G. Balakrishnan, T. Rajendran, K. Senthil Murugan, M. Ganesan, V. K. Sivasubramanian and S. Rajagopal, *J. Lumin.*, 2019, **205**, 51.
- D. S. Reddy, M. Kongot, S. P. Netalkar, M. M. Kurjogi and A. Kumar, *Eur. J. Med. Chem.*, 2018, **150**, 864.
- V. Sharma, P. Cantero-López, O. Yañez-Osses, C. Rojas-fuentes and A. Kumar, *J. Mol. Liq.*, 2018, **271**, 443.
- F. Shen, Z. B. Ou, Y. J. Liu, W. Liu, B. F. Wang, Z. W. Mao and X. Y. Le, *Inorg. Chim. Acta*, 2017, **465**, 1.
- S. Dang, L. N. Sun, S. Y. Song, H. J. Zhang, G. L. Zheng, Y. F. Bi, H. D. Guo, Z. Y. Guo and J. Feng, *Inorg. Chem. Commun.*, 2008, **11**, 531.
- L. Palatinus and G. Chapuis, *J. Appl. Crystallogr.*, 2007, **40**, 786.
- V. Petricek, M. Dusek and L. Palatinus, *Z. Kristallogr.*, 2014, **229**, 345.
- M. Shahnawaz Khan, M. Khalid, M. Shahwaz Ahmad, M. Ahmad, M. Ashafaq, R. Arif and M. Shahid, *J. Mol. Struct.*, 2019, **1175**, 889.
- P. Singla, V. Luxami and K. Paul, *Eur. J. Med. Chem.*, 2016, **117**, 59.
- G. M. Morris, D. S. Goodsell, R. S. Halliday, R. Huey, W. E. Hart, R. K. Belew and A. J. Olson, *J. Comput. Chem.*, 1998, **19**, 1639.
- T. T. Zhao, X. Lu, X. H. Yang, L. M. Wang, X. Li, Z. C. Wang, H. B. Gong and H. L. Zhu, *Bioorg. Med. Chem.*, 2012, **20**, 3233.
- L. Basiri, G. Rajabzadeh and A. Bostan, *LWT-Food Sci. Technol.*, 2017, **84**, 471.
- S. Dang, L. N. Sun, S. Y. Song, H. J. Zhang, G. L. Zheng, Y. F. Bi, H. D. Guo, Z. Y. Guo and J. Feng, *Inorg. Chem. Commun.*, 2008, **11**, 531.
- Y. C. Liu and Z. Y. Yang, *J. Organomet. Chem.*, 2009, **694**, 3091.
- Sh. Jahani, M. Noroozifar, M. Khorasani-Motlagh, M. Torkzadeh-Mahani and M. Adeli-Sardou, *J. Biomol. Struct. Dyn.*, 2019, **37**, 4437.
- S. Kashanian, M. B. Gholivand, F. Ahmadi, A. Taravati and A. Hosseinzadeh Colagar, *Spectrochim. Acta, Part A*, 2007, **67**, 472.
- F. Chen, Z. Xu, P. Xi, X. Liu and Z. Zeng, *Anal. Sci.*, 2009, **25**, 359.
- Sh. Jahani, M. Khorasani-Motlagh and M. Noroozifar, *J. Biomol. Struct. Dyn.*, 2016, **34**, 612.
- L. Guo, B. Qiu and G. Chen, *Anal. Chim. Acta*, 2007, **588**, 123.
- S. Niroomand, M. Khorasani-Motlagh, M. Noroozifar, Sh. Jahani and A. Moodi, *J. Mol. Struct.*, 2017, **1130**, 940.
- F. Sama, M. Raizada, M. Ashafaq, M. Naqi Ahmad, I. Mantasha, I. Khushboo, M. Shahid, R. Arif, N. A. Shah and H. A. M. Saleh, *J. Mol. Struct.*, 2019, **1176**, 283.
- B. Barut, U. Demirbaş, A. Şenocak, A. Özel and H. Kantekin, *Synth. Met.*, 2017, **229**, 22.
- S. Nafisi and T. S. Vishkaee, *J. Photochem. Photobiol., B*, 2011, **105**, 34.
- S. Tabassum, M. Ahmad, M. Afzal, M. Zaki and P. K. Bharadwaj, *J. Photochem. Photobiol., B*, 2014, **140**, 321.
- M. Anjomshoa and M. Torkzadeh-Mahani, *Spectrochim. Acta, Part A*, 2015, **150**, 390.
- C. L. Zhang, Y. X. Liu, X. M. Zhang, S. Chen, F. Shen, Y. H. Xiong, W. Liu, Z. W. Mao and X. Y. Le, *Mater. Sci. Eng. C*, 2018, **91**, 414.



- 47 V. Arumugam, R. Rajamanikandan, M. Ilanchelian, K. G. Moodley and G. G. Redhi, *Spectrochim. Acta, Part A*, 2019, **210**, 299.
- 48 A. V. Protas, E. A. Popova, O. V. Mikolaichuk, Y. B. Porozov, A. R. Mehtive, I. Ott, G. V. Alekseev, N. A. Kasyanenko and R. E. Trifonov, *Inorg. Chim. Acta*, 2018, **473**, 133.
- 49 F. C. Yang, K. H. Wu, W. P. Lin and M. K. Hu, *Microporous Mesoporous Mater.*, 2009, **118**, 467.
- 50 N. P. Priya, S. V. Arunachalam, N. Sathya, V. Chinnusamy and C. Jayabalakrishnan, *Transition Met. Chem.*, 2009, **34**, 437.
- 51 S. Niroomand, M. Khorasani-Motlagh and A. Moodi, *J. Photochem. Photobiol., B*, 2012, **117**, 132.
- 52 Z. Aramesh-Boroujeni, M. Khorasani-Motlagh and M. Noroozifar, *J. Biomol. Struct. Dyn.*, 2016, **34**, 414.
- 53 Z. Aramesh-Boroujeni, A. K. Bordbar, M. Khorasani-Motlagh, E. Sattarinezhad, N. Fani and M. Noroozifar, *J. Biomol. Struct. Dyn.*, 2019, **37**, 1438.
- 54 Z. Aramesh-Boroujeni, Sh. Jahani, M. Khorasani-Motlagh, K. Kerman and M. Noroozifar, *J. Biomol. Struct. Dyn.*, 2020, **38**, 1711.
- 55 Z. Aramesh-Boroujeni, S. Jahani, M. Khorasani-Motlagh, K. Kerman, N. Aramesh, S. Asadpour and M. Noroozifar, *J. Biomol. Struct. Dyn.*, 2019, **1**, DOI: 10.1080/07391102.2019.1689170.

